








RESEARCH ARTICLE | DECEMBER 06 2024

The role of the dopant in the electronic structure of erbium-doped TiO_2 for quantum emitters

J. B. Martins ; G. Grant ; D. Haskel ; G. E. Sterbinsky ; I. Masiulionis ; K. E. Sautter ; E. Karapetrova; S. Guha ; J. W. Freeland 



APL Mater. 12, 121110 (2024)
<https://doi.org/10.1063/5.0241141>



Articles You May Be Interested In

Transforming underground to surface mining operation – A geotechnical perspective from case study

AIP Conference Proceedings (November 2021)

Monthly prediction of rainfall in nickel mine area with artificial neural network

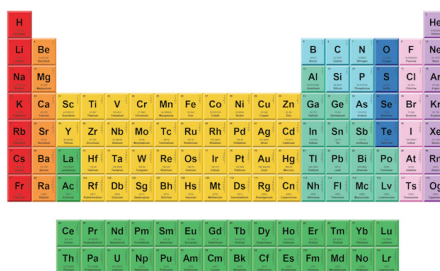
AIP Conference Proceedings (November 2021)

Estimation of Karts groundwater based on geophysical methods in the Monggol Village, Saptosari District, Gunungkidul Regency

AIP Conference Proceedings (November 2021)



Now Invent.™



American Elements
 Opens a World of Possibilities

...Now Invent!

www.americanelements.com

© 2021-2024 American Elements is a U.S. Registered Trademark

The role of the dopant in the electronic structure of erbium-doped TiO₂ for quantum emitters

Cite as: APL Mater. 12, 121110 (2024); doi: 10.1063/5.0241141

Submitted: 28 September 2024 • Accepted: 22 November 2024 •

Published Online: 6 December 2024



J. B. Martins,^{1,a)} G. Grant,^{2,b)} D. Haskel,¹ G. E. Sterbinsky,¹ I. Masiulionis,^{2,b)} K. E. Sautter,^{2,b)} E. Karapetrova,¹ S. Guha,^{2,b)} and J. W. Freeland¹

AFFILIATIONS

¹X-ray Science Division, Argonne National Laboratory, Lemont, Illinois 60439, USA

²Pritzker School of Molecular Engineering, University of Chicago, Chicago, Illinois 60637, USA

^{a)}Author to whom correspondence should be addressed: jbarbosamartins@anl.gov

^{b)}Also at: Materials Science Division, Argonne National Laboratory, Lemont, IL 60439, USA.

ABSTRACT

Erbium-doped TiO₂ materials are promising candidates for advancing quantum technologies, necessitating a thorough understanding of their electronic and crystal structures to tailor their properties and enhance coherence times. This study explored epitaxial erbium-doped rutile TiO₂ films deposited on r-sapphire substrates using molecular beam epitaxy. Photoluminescence excitation spectroscopy demonstrated decreasing photoluminescence lifetimes with erbium doping, indicating limited optical coherence times. Lattice distortions associated with Er³⁺ were probed by x-ray absorption spectroscopy, indicating that erbium primarily occupies Ti⁴⁺ sites and influences oxygen vacancies. Significant lattice distortions in the higher-order shells and apparent full coordination around erbium suggest that additional defects are likely prevalent in these regions. These findings indicate that defects contribute to limited coherence times by introducing alternative decay pathways, leading to shorter photoluminescence lifetimes.

© 2024 Author(s). All article content, except where otherwise noted, is licensed under a Creative Commons Attribution-NonCommercial-NoDerivs 4.0 International (CC BY-NC-ND) license (<https://creativecommons.org/licenses/by-nc-nd/4.0/>). <https://doi.org/10.1063/5.0241141>

I. INTRODUCTION

The relentless growth in data storage and the continuous trend of device miniaturization has driven technological progress to approach the quantum limit.^{1,2} Quantum information science (QIS), grounded in the principles of quantum mechanics, emerges as a groundbreaking solution for efficient data handling, secure information exchange, and long-distance communication while ensuring data integrity.^{3,4} At the heart of quantum technologies lies the manipulation of qubits, the fundamental units of quantum information.^{4,5} Quantum coherence plays a crucial role in realizing quantum technologies,⁶ which enables qubits to maintain the superposition of quantum states. However, the challenge lies in preserving coherence, which is limited by the inherent susceptibility to environmental influences. Therefore, ensuring the prolonged persistence of quantum states in superposition (i.e., long coherence time) is essential for successfully implementing quantum information technologies.^{5,6}

Solid-state spin qubits show significant promise among the candidates for QIS applications, owing to their compatibility with

conventional microelectronics.^{5,6} Nevertheless, the properties of solid-state spin qubits are linked to their crystal host, necessitating material engineering to enhance the quantum emitter's properties and mitigate decoherence sources such as charge carriers or phonons. Among potential candidates, rare-earth ions (REIs) in solid-state systems stand out.⁷ In particular, the trivalent erbium ion (Er³⁺) is noteworthy for its optical 4f–4f transition within telecom-C band, aligning with the low-loss transmission in optical fibers, making it an ideal quantum emitter for quantum network systems.^{8–13} Selecting the optimal crystal host for REIs in QIS involves considering factors such as low nuclear and electron spin concentrations, nonpolar symmetry, and a large bandgap.^{6,13,14} These factors are instrumental in not only enhancing optical transitions but also in mitigating local effects in the vicinity of REIs, thereby addressing coherence issues effectively. Previous studies identified TiO₂ as a promising host for Er₃₊, with the rutile and anatase phases being particularly stable.^{15,16} Recent research on Er-doped TiO₂ films and bulk crystals has demonstrated narrow optical inhomogeneous linewidths, underscoring the importance of buffer and capping layers in enhancing optical properties.^{15,17} Despite

these advancements, further understanding is needed on how Er^{3+} dopants influence the TiO_2 host lattice's electronic and crystal structure.

This investigation focuses on epitaxial erbium-doped rutile TiO_2 thin films grown on *r*-plane sapphire substrates, aiming to explore how erbium incorporation affects the material's optical properties. We employed spectroscopy and diffraction techniques to correlate structural modifications with variations in excited state lifetimes. The selection of sapphire as the substrate was deliberate, as it enables the formation of high-quality single-crystal rutile TiO_2 . X-ray diffraction (XRD) confirmed the persistence of single crystallinity despite doping. Variations on the Er^{3+} photoluminescence lifetimes, which set the upper bounds for optical coherence times, were assessed using photoluminescence excitation (PLE) spectroscopy revealing a downward trend with increasing doping. In addition, information on local coordination, lattice distortion, and chemical environment near erbium sites was probed using x-ray absorption spectroscopy (XAS) and extended x-ray absorption fine structure (EXAFS). The analyses indicate that doping increases oxygen vacancy defect density within TiO_2 . Furthermore, they suggest that erbium ions are fully coordinated, indicating redistribution of oxygen vacancies away from the Er sites. This increase in additional defect density is likely to limit coherence by introducing alternative decay pathways upon Er^{3+} excitation.

II. METHODS

A. Samples Growth

Epitaxial $\text{Er}:\text{TiO}_2$ thin films with thicknesses of 65 nm were deposited using a Riber C21 DZ Cluster molecular beam epitaxy (MBE) system. Titanium tetraisopropoxide (TTIP) from Sigma-Aldrich with a purity of 99.999% (trace metal basis) was the titanium precursor as in the TTIP-based MBE of TiO_2 detailed elsewhere.¹⁸ Growths were carried out on an *r*-plane (102) sapphire substrate at 640 °C temperature, oxygen partial pressure of 7×10^{-6} Torr, and a TTIP beam-equivalent flux of 3.5×10^{-6} . The growth rate was 32.5 nm per hour. *In situ* erbium (Er) doping (20, 200, and 500 ppm) using metallic Er was carried out by a high-temperature (860–990 °C) effusion cell.

B. Structural and optical characterization

Single crystal x-ray diffraction characterization was carried out at the 33BM beamline of the Advanced Photon Source (APS) at photon energy of 20 keV. PLE spectroscopy was performed in a custom confocal microscopy setup designed for telecom C-band measurement of thin films, with samples mounted in a cryostat at 3.5 K (s50 Cryostation, Montana Instruments). A tunable 1.5 μm laser illuminated the samples for 1.5 ms using pulses shaped by acousto-optic modulators. Emission from the samples subsequent to excitation was then collected by a Quantum Opus superconducting nanowire single photon detector (SNSPD) for 3 ms collection intervals. Sweeping the excitation laser wavelength resulted in a PLE spectrum and excited state lifetime measurements at each wavelength for each measured sample. Additional information on this experimental setup is given in detail elsewhere.¹² XAS measurements were conducted at O *K*-edge, Ti *L*-edge, and Er *M*₅-edges at the 29ID beamline at the Advanced Photon Source (APS). The

beam was directed along surface normal, and the spectra were averaged over the acquired horizontal and vertical polarization to ensure orientation-independent assessment of the local environment. The EXAFS measurements were performed at the 20-BM beamline of the APS. Data collection was conducted in grazing incidence geometry, with an angle of incidence of a few degrees and with linear x-ray polarization in the plane of the film. The sample was rotated about the film surface normal to average in-plane polarizations. The temperature was maintained at 300 K throughout the entire experiment. Since the [101] direction is along the surface normal, separate FEFF8 simulations were carried out with linear polarization along orthogonal in-plane $[-101]$ and $[010]$ directions to obtain theoretical phase shifts and scattering amplitudes.¹⁹

III. RESULTS AND DISCUSSION

A. Characterization of epitaxial $\text{Er}:\text{TiO}_2$ films by single crystal x-ray diffraction

Figure 1 shows the single crystal x-ray diffraction spectra, confirming the $(012)_{\text{Al}_2\text{O}_3}$ direction normal to the *r*-plane surface through the specular (0, K, 2K) scan. The film shows a main peak of $(101)_{\text{TiO}_2}$ film orientation on the *r*-plane surface consistent with previous literature.^{20,21} Positions of the peaks are roughly equivalent with the expected bulk values indicating that the films are relaxed. The lattice parameter approximates that of bulk TiO_2 . As was noted in a previous work,²⁰ the matching of the symmetry between the $(012)_{\text{Al}_2\text{O}_3}$ and $(101)_{\text{TiO}_2}$ planes leads to a twinned structure with alternating domains on 10's of nm length scales. These domains likely lead to a relaxation to the bulk lattice values due to the high-density of domain walls. In addition, all films exhibit a minority (301) orientation, which may result from the high density of twin domains. No systematic behavior with doping was observed, suggesting that the minority (301) orientation is unrelated to doping.

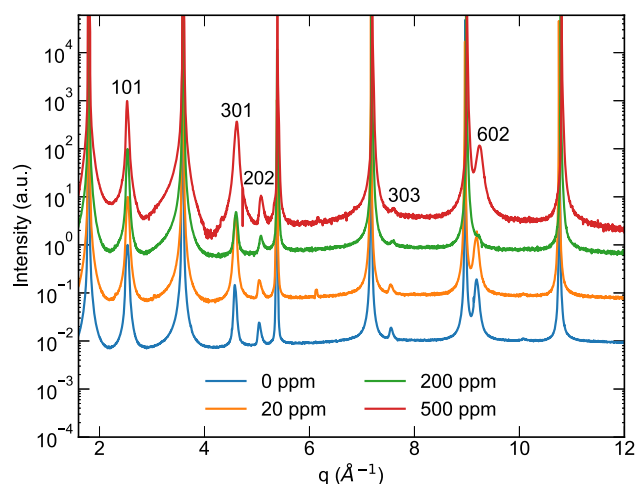


FIG. 1. (101) Rutile TiO_2 grown on the (012) surface of sapphire, exhibiting primary (101) orientation with a minor (<10%) phase with a (301) orientation.

B. Impact of erbium concentration on optical properties

The impact of increasing Er^{3+} dopant density on the rutile TiO_2 host lattice was investigated by optical characterization of the thin film samples performed via time-resolved PLE spectroscopy. Figure 2(a) shows the resulting absorption spectra near $1.5 \mu\text{m}$ resonance for the series of single crystal erbium-doped rutile TiO_2 films. The ground ($^4I_{15/2}$) and excited ($^4I_{13/2}$) electronic states of Er^{3+} in rutile fully split into eight (Z_{1-8}) and seven (Y_{1-7}) Kramers' doublets, respectively [Fig. 2(b)],¹⁵ due to the D_{2h} point symmetry for Er^{3+} occupying Ti^{4+} sites in rutile TiO_2 . The growing background toward lower wavelengths stems from the dopant-driven introduction of additional defects and disorder into the lattice, resulting in the available crystal field transitions broadening significantly.²² At high doping levels (such as the 500 ppm sample in this work), the inhomogeneous linewidths are broad enough that individual peaks become more difficult to resolve.

We focus our discussion on the peak highlighted by a vertical dashed line ($\sim 1520 \text{ nm}$), which corresponds to the technologically prescient $\text{Er}^{3+} Z_1 \rightarrow Y_1$ transition in rutile-phase TiO_2 .¹⁵ The narrowest observed inhomogeneous linewidth in this set of thin films is $\sim 50 \text{ GHz}$, found in the sample doped with 20 ppm erbium. The inhomogeneous linewidth increases with higher dopant concentrations, with the broadening of the linewidth attributable to electric fields generated by charged defects near the Er^{3+} sites, including negatively charged point defects resulting from Er^{3+} substituting Ti^{4+} sites (i.e., the negative charge upon replacement of Ti^{4+} to Er^{3+}) and positively charged oxygen vacancy point defects.^{17,23–26}

The lifetime of the excited state sets an upper limit for the coherence time, and shorter lifetimes may also be an indicator of lower quantum efficiency. Therefore, identifying dopant-driven variation in the excited state lifetime is critical in assessing the material's quality as a host for quantum processes, given the intentional introduction of dopants, such as Er^{3+} , as necessary to facilitate these processes. Understanding the nuances of local electronic and crystal structures is pivotal for comprehending the alterations in the inherent optical properties of Er-doped rutile TiO_2 with varying erbium concentrations.

TABLE I. Er^{3+} photoluminescence lifetimes and estimated quantum efficiencies for Er-doped rutile TiO_2 samples.

Er concentration (ppm)	Lifetime (ms)	Quantum efficiency
20	2.1 (3)	0.40 (6)
200	0.99 (2)	0.189 (4)
500	0.63 (1)	0.120 (2)

The photoluminescence lifetimes at the highlighted peak (Table I) exhibit a dopant-driven decreasing trend. This shortening of lifetime is consistent with prior observations in CeO_2 with increasing erbium doping, where the decrease is attributed to the introduction of defects. While the exact nature of these defects remains uncertain, they likely introduce non-radiative or quenching pathways that shorten the photoluminescence lifetimes.²² If the defects were strictly localized to individual Er sites, their interaction would be limited and neither significant linewidth broadening nor a pronounced reduction in lifetime would be expected. However, the impact of these defects is significant, and is emphasized by the decrease in quantum efficiency with higher doping (also presented in Table I), estimated based on the longest observed excited state lifetime of $Y_1 \rightarrow Z_1$ for Er-doped rutile TiO_2 in the literature, of $5.25 \pm 0.03 \text{ ms}$.¹⁵ The increased linewidth and shorter photoluminescence lifetimes at higher dopant concentrations suggest that the defects surrounding the Er^{3+} sites are not confined to the immediate vicinity but instead form more extended distributions. These extended defects likely modify the local crystal field around the Er ions, thereby influencing the observed optical properties.

C. Influence of erbium on the electronic structure of TiO_2 host lattice

To further elucidate these modifications, we employed XAS to investigate erbium-induced changes in the local electronic structure within the crystal lattice. Starting with oxygen spectroscopy, the O K-edge spectra shown in Fig. 3(a) are a result of electronic

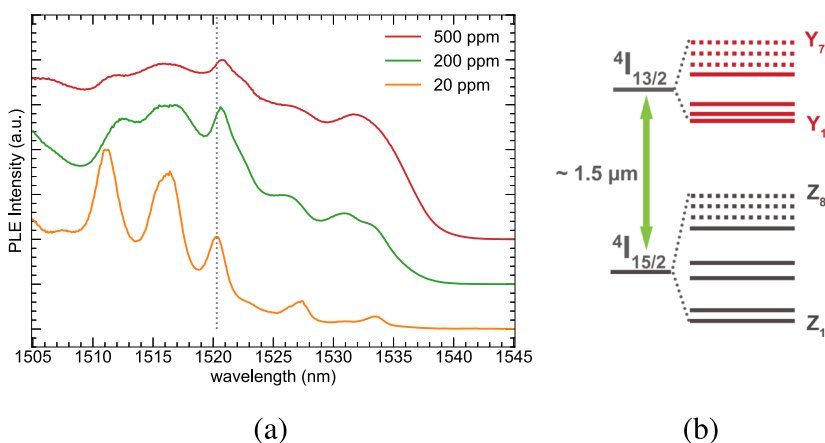


FIG. 2. (a) PLE spectra for the set of Er-doped TiO_2 thin films. (b) Energy level diagram for $^4I_{15/2} \rightarrow ^4I_{13/2}$ transition in Er^{3+} ion.

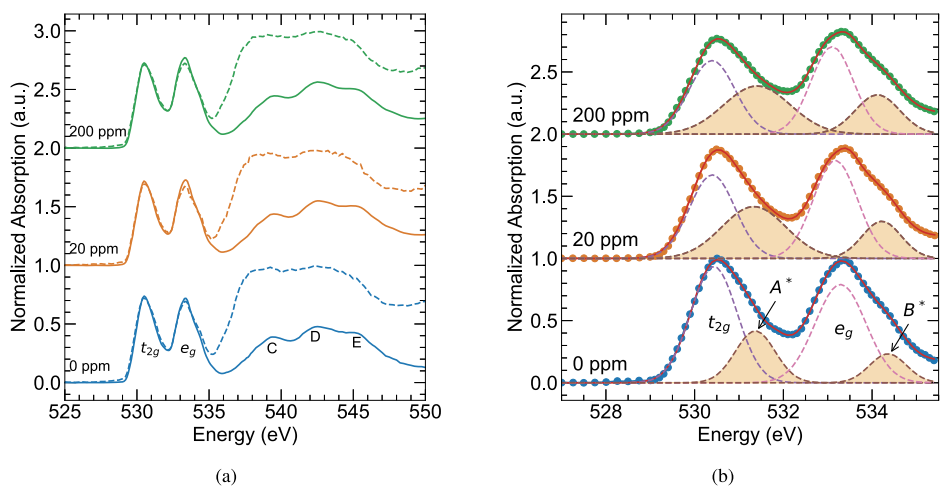


FIG. 3. (a) XAS O *K*-edge spectra for undoped (0 ppm) and Er-doped (20 and 200 ppm) TiO₂ films, measured via surface-sensitive TEY mode (solid lines) and bulk-sensitive FY mode (dashed lines). (b) Gaussian fit analysis of TEY spectra depicting the pre-peaks corresponding to electron transitions from O 1s shell into unoccupied O 2p orbitals hybridized with Ti *t*_{2g} and *e*_g orbitals, respectively, and adjacent features *A*^{*} and *B*^{*} indicating oxygen vacancies.³²

transitions from O(1s) states to unoccupied O(2p) states. The spectra were acquired simultaneously in both total electron yield (TEY) mode, using the sample photocurrent method, and fluorescence yield (FY) mode, using an energy-discriminating silicon drift diode detector (Vortex) coupled with a multi-channel analyzer (MCA). The TEY and FY spectra are represented by the solid and dashed lines, respectively. The primary distinction between TEY and FY acquisition modes lies in their depth sensitivity, with TEY being more surface-sensitive and FY more bulk-sensitive. TiO₂ consists of a central Ti⁴⁺ ion surrounded by six O²⁻ ions arranged as a distorted TiO₆ octahedron due to the tetragonal symmetry of the crystal structure. This distortion causes the crystal field splitting of the Ti 3*d* orbitals into lower-energy *t*_{2g} states and higher-energy *e*_g states.^{27–29} Geometrically, the *e*_g orbitals from Ti point toward the O 2*p* orbitals, while the *t*_{2g} lobes point between the O atoms leading to strong hybridization between O(2*p*) and Ti(3*d*) orbitals. The significant hybridization leads to two distinguishable pre-peaks at ~530 and 533 eV labeled as *t*_{2g} and *e*_g, respectively. Moreover, three distinct features at higher energies, with peaks around 539, 542, and 545 eV, denoted as C, D, and E, respectively, correspond to delocalized O(2*p*)–Ti(4*s*) and O(2*p*)–Ti(3*d*) hybridized states and are a fingerprint of the rutile phase in TiO₂.³⁰

Two notable trends emerge from comparing the TEY and FY spectra. First, the intensity ratio of the *t*_{2g} and *e*_g pre-peaks varies with increasing erbium concentration in both TEY and FY spectra, suggesting that these variations are not confined to the surface and exist in the bulk of the film as well. Second, the FY spectra, which provide greater depth sensitivity than TEY, display broader peaks between 538 and 545 eV. This broadening is attributed to contributions from the sapphire substrate.³¹ Due to the strong hybridization between O(2*p*) and Ti(3*d*) orbitals, the *t*_{2g} and *e*_g pre-peaks in the O *K*-edge spectra are expected to be highly sensitive to changes in the electronic structure. Thus, the fitting analysis shown in Fig. 3(b) focused on the two pre-peaks in the TEY spectra to gain insights into the electronic structure of the host lattice. Gaussian functions were fitted to the spectra, revealing two distinct features labeled as *A*^{*} and *B*^{*}, adjacent to the main *t*_{2g} and *e*_g peaks, respectively. These adjacent features are ~1 eV blueshifted from the main peaks and can be

attributed to modifications in the electronic structure of the rutile lattice related to oxygen vacancies.³²

Notably, the *A*^{*} and *B*^{*} features are present even in the undoped sample, indicating non-stoichiometric TiO₂. Their area increases with erbium doping, as presented in Table II. Native point defects, such as neutral or charged oxygen vacancies, are common in wide-bandgap metal oxides such as TiO₂.^{33,34} The increase in *A*^{*} and *B*^{*} areas with doping suggests that erbium introduces new oxygen vacancies into the lattice. Each Er ion is expected to create only half an oxygen vacancy to balance the charge (i.e., one O_v²⁺ vacancy balances the charge of two Er³⁺ ions). Despite this, the substantial increase in *A*^{*} and *B*^{*} peak areas implies that defects around different Er sites likely overlap or interact. This overlap leads to significant changes in the XAS spectra, even at low Er concentrations, suggesting that the defects are likely not isolated but form a more extensive network within the material. Moreover, the erbium-driven increase in *A*^{*} and *B*^{*} areas is accompanied by a decrease in the *t*_{2g} and *e*_g peak areas, reflecting disruptions in the local electronic structure. The creation of new oxygen vacancies disrupts the strong hybridization between O(2*p*) and Ti(3*d*) orbitals, leading to reduced overlap and thus smaller *t*_{2g} and *e*_g peak areas.

Similar to the O *K*-edge, the Ti *L*-edge XAS spectra are sensitive to changes in electronic structure due to the hybridization of O(2*p*) and Ti(3*d*) orbitals. Therefore, the Ti *L*-edge was probed using TEY

TABLE II. Peak areas obtained from Gaussian fitting analysis of pre-peaks in XANES O *K*-edge spectra. Two main trends are observed. First, the overall decrease in areas of the main *t*_{2g} and *e*_g pre-peaks with increasing erbium concentration. In contrast, erbium-driven increasing in the *A*^{*} and *B*^{*} areas suggest the generation of oxygen vacancies within the host lattice.

Er concentration (ppm)	Peak area (a.u.)			
	<i>t</i> _{2g}	<i>A</i> [*]	<i>e</i> _g	<i>B</i> [*]
0	1.22 (14)	0.47 (9)	1.13 (8)	0.24 (7)
20	0.86 (14)	0.76 (9)	0.98 (8)	0.33 (7)
200	0.77 (14)	0.73 (9)	0.84 (8)	0.40 (7)

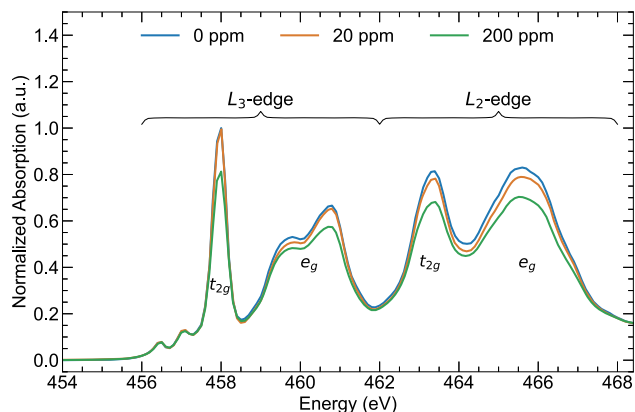


FIG. 4. Ti L-edge spectra for undoped (0 ppm) and Er-doped TiO₂ samples (20 and 200 ppm).

mode to investigate possible dopant-induced modifications in the electronic structure (Fig. 4). The fine structure in the L_3 and L_2 edges results from the breaking of degenerate electronic orbitals by the lattice crystal field, leading to the splitting of 3d states into threefold t_{2g} and twofold degenerate e_g states. Further distortion from the lattice environment introduces additional splitting, which is pronounced at the L_3 -edge. The first two weak pre-edge peaks are attributed to the combined effects of particle-hole coupling and crystal field splitting. These features exhibit low intensity due to partial screening of the core hole by surrounding electrons, which is influenced by the localized electronic environment and transition metal oxidation state, as discussed in previous studies.^{35,36} The intense, narrow peak around 458 eV corresponds to the t_{2g} state, while the e_g states split into two peaks due to the distortion in the TiO₆ octahedra. This distortion leads to an inversion of the relative intensities of the e_g peaks in the XAS spectra for different TiO₂ polymorphs. As a result, the relative intensity ratio of the e_g peaks serves as a distinct fingerprint for identifying TiO₂ polymorphs, and in this case, it is consistent with the rutile phase.²⁸

Expected consequences of doping include charge compensation through the formation of additional defects, such as oxygen vacancies and Ti³⁺, as well as distortions of the host lattice.^{26,37,38} Prior investigations on Cr-doped rutile TiO₂ highlighted the critical role of oxygen point defects in stabilizing Cr³⁺ ions, particularly through the formation of complex defects involving two Cr atoms and one oxygen vacancy.³⁸ This stabilization is associated with distortions in the crystal lattice due to the elongation of Ti–O bonds, which affect the Ti e_g orbitals. These orbitals are highly sensitive to changes in the local environment because they interact directly with the 2p orbitals of the surrounding O atoms. As the local symmetry and crystal field around the Ti ions change, the energy levels of the e_g orbitals shift accordingly. In our study, the low concentration of Er³⁺ dopant—on the order of hundreds of parts per million (ppm)—makes it challenging to observe significant lattice distortions or prominent features associated with e_g orbital splitting or Ti³⁺-related signals. However, comparisons between undoped and doped samples reveal an overall decrease in spectral intensity with Er doping, suggesting that the dopant induces changes in the local

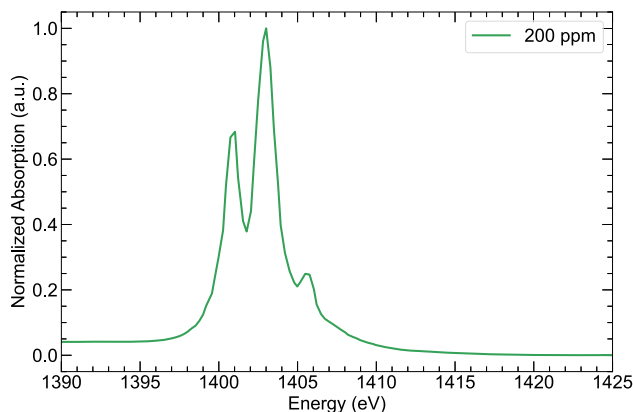


FIG. 5. XAS spectrum at the Er M_5 edge for 200 ppm doped Er:TiO₂.

electronic environment around the Ti ions. These changes may arise from slight distortions in the Ti–O coordination environment, which, in turn, alter the crystal field and electronic structure of the Ti sites.

To gain deeper insight into how the dopant affects the formation of additional defects within the host lattice, erbium spectroscopy was performed. The XAS spectrum at the Er M_5 -edge (Fig. 5) exhibits three distinct peaks corresponding to $3d \rightarrow 4f$ transitions. These transitions, characterized by changes in the total angular momentum quantum number ($\Delta l = 0, \pm 1$), are indicative of erbium in the trivalent state.³⁹

D. Structural distortions upon erbium incorporation into TiO₂

The local environment around the Er³⁺ sites was further examined using EXAFS at the Er L -edge and Ti K -edge, as shown in Fig. 6. A comparison of the experimental data with FEFF8 simulations is shown in Figs. 6(a) and 6(d), where the Fourier-transformed (FT) XAFS data for the Ti K -edge and Er L_3 -edge, respectively, are represented by the solid lines.

These comparisons revealed significant differences, particularly in the FT Er L_3 -edge spectra, where a marked shift toward higher distances in the first shell was observed, along with a notable suppression in the higher-R structure. These observations suggest alterations in the local structure around erbium, such as bond length variations or changes in coordination numbers at greater distances. The experimental data, acquired at 300 K, were scaled by a factor of 2 in these two plots to better match with simulations conducted at 0 K.

Figures 6(e) and 6(b) show FT XAFS data and fits for Er L_3 -edge and Ti K -edge, respectively. Each polarization contribution was equally weighted (0.5) in the fits to account for in-plane polarization and sample spin, employed during the data acquisition to reduce Bragg peak artifacts in the experiment. The analysis involved simultaneous fitting of data weighted by different k -weights to minimize correlations between coordination number and the Debye–Waller factor (σ^2). The small nominal split of 0.04 Å in first shell Ti/Er–O

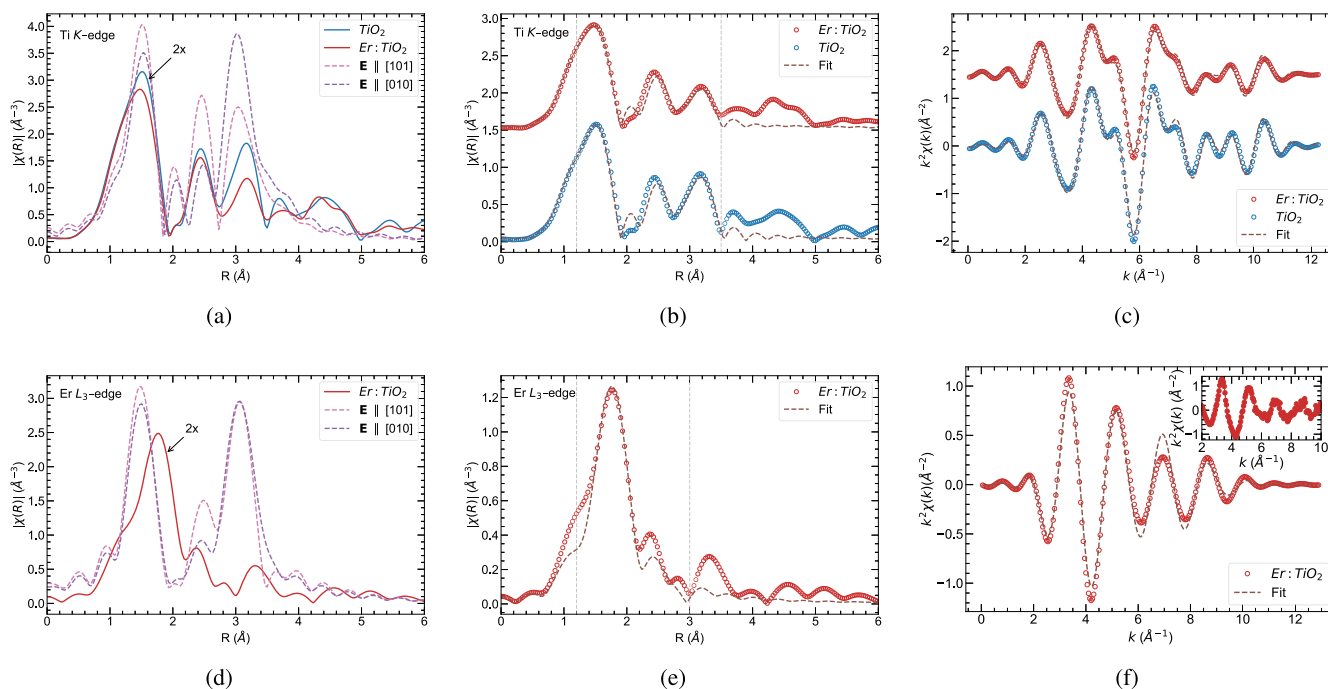


FIG. 6. Fourier-transformed (a) Ti K-edge and (d) Er L_3 -edge XAS spectra of undoped (solid blue) and 500 ppm Er-doped (solid red) TiO_2 samples. The k range used in the FTs was $[2-11] \text{ \AA}^{-1}$ and $[2-10] \text{ \AA}^{-1}$ for Ti K and Er L_3 -edges, respectively. The dashed curves represent FEFF8 simulations for electric field polarizations along the [010] and $[-101]$ directions. Fitted Fourier-transformed (b) Ti K-edge spectra for undoped TiO_2 (blue circles) and 500 ppm Er-doped TiO_2 (red circles), and (e) Er L_3 -edge spectrum for 500 ppm Er-doped TiO_2 . The vertical dashed lines indicate regions used in the real-space fits. Panels (c) and (f) show the back Fourier transform of data and fits in the real-space region marked by the vertical lines for the Ti K-edge and Er L_3 -edge, respectively. The inset plot shows the unfiltered, k^2 -weighted EXAFS spectrum at the Er L_3 -edge within the k -range used in the FT, highlighting raw spectral features prior to filtering.

distances cannot be resolved with the limited k -range of the XAFS data ($k_{\text{max}} \sim 10 \text{ \AA}^{-1}$) hence the fitted bond length correction was forced to be proportional to the nominal bond lengths. Similarly, coordination numbers of split distances were fitted while maintaining their ratio fixed to nominal values. The FT Er L_3 -edge spectrum [Fig. 6(e)] revealed erbium coordinated to oxygen for the first shell (Er–O), with an expanded bond length of 2.20 \AA (Table III). This distance is significantly larger than the corresponding Ti–O₍₁₎ bond length of 1.92 \AA observed in the Ti K-edge analysis, indicating a local expansion in the lattice around the erbium dopant. In addition, the presence of Ti neighbors at a distance of 3.09 \AA in the second shell suggests that Er^{3+} is occupying Ti^{4+} lattice sites and is consistent with previous ESR-based investigations on Er-doped rutile TiO_2 .¹⁵

The significant local expansion observed around Er aligns with the difference in ionic radii between Er^{3+} and Ti^{4+} . The theoretical difference in ionic radii is 0.29 \AA ($0.89-0.605 \text{ \AA}$),⁴⁰ which closely matches the experimental local expansion of 0.28 \AA , as indicated by the difference between the Er–O₍₁₎ bond length (2.20 \AA) and the Ti–O₍₁₎ bond length (1.92 \AA) presented in Table III. This close agreement between theoretical and experimental values, combined with nominal ($N = 2$) Er–Ti coordination in the second shell at a bond distance of 3.09 \AA , supports the hypothesis that Er^{3+} is substituting at Ti^{4+} sites, albeit with significant lattice distortion

especially at higher order shells. Interestingly, the amplitude of Ti K-edge XAFS is somewhat reduced in the doped sample, despite the rather low doping level of 500 ppm, indicating that structural distortions around Er ions are extended, affecting a larger % of Ti ions. These results can also be correlated with the overall intensity decreasing in Ti L -edge XAS spectra with doping shown in Fig. 4, as erbium ions appear to cause lattice distortions. The Ti K-edge analysis [Fig. 6(b)] for the undoped sample (blue circles) yielded fitted distances closely resembling the nominal TiO_2 structure. Small differences were observed for the doped sample (red circles), although signatures of increased disorder are present particularly at the longer Ti–Ti correlations (Table III). The same amplitude reduction factor (S_0^2) of 0.93 was used for both the Ti K-edge and Er L_3 -edge fits to ensure consistency across the analyses.

The substitution of Ti^{4+} by Er^{3+} ions raises important questions about the mechanisms of charge compensation that stabilize the dopant within the host structure. The increased area of the A^* and B^* features in the O K-edge spectra, which are associated with oxygen vacancies, suggests that these vacancies play a key role in compensating for the charge imbalance introduced by Er^{3+} ions, thereby maintaining charge neutrality.^{41,42} EXAFS analysis indicates that the first coordination shell of both Er^{3+} and Ti^{4+} remains fully occupied by oxygen, as reflected by coordination numbers close to 6

TABLE III. Structural parameters from Er and Ti XAFS fitting analyses. The amplitude reduction factor (S_0^2) of 0.93 was determined from Ti K-edge fits and fixed in Er L_3 -edge fits. FEFF8 simulations used nominal TiO_2 bond lengths. The footnote values correspond to the nominal Ti–O and Ti–Ti bond lengths. Lattice distortions were accounted for during fitting, reflecting the observed disorder in higher-R shells. Coordination numbers for higher-R shells (i.e., Ti–Ti₍₂₎ and Er–Ti₍₁₎) are absent due to significant disorder and weak scattering amplitudes.

Probed atom	Bond	Bond length (Å)		Debye waller factor (Å ²)		Coordination number	
		0 ppm	500 ppm	0 ppm	500 ppm	0 ppm	500 ppm
Ti K-edge	Ti–O ₍₁₎	1.934 (5) ^a	1.92 (1)	0.0055 (5)	0.0060 (1)	4.1 (2)	4.1 (2)
	Ti–O ₍₂₎	1.978 (5) ^b	1.96 (1)	0.0055 (5)	0.0060 (1)	2.1 (1)	2.1 (1)
	Ti–Ti ₍₁₎	3.02 (1) ^c	3.00 (3)	0.0040 (1)	0.0030 (1)	2 ^d	2 ^d
	Ti–Ti ₍₂₎	3.61 (1) ^e	3.62 (2)	0.0062 (9)	0.0010 (4)	8 ^d	8 ^d
Er L_3 -edge	Er–O ₍₁₎	...	2.20 (1)	...	0.0056 (7)	...	4.3 (2)
	Er–O ₍₂₎	...	2.25 (1)	...	0.0056 (7)	...	2.1 (1)
	Er–Ti ₍₁₎	...	3.09 (3)	...	0.0140 (5)	...	2 ^d

^a1944 Å.
^b1988 Å.
^c2959 Å.
^dFixed.
^e357 Å.

for both species. In particular, the coordination number of Er–O is 6.4 (3) (Table III), while the coordination number for Ti–O is 6.2 (3), supporting full occupation in the first shell. However, the error bars of around 5% in the coordination number allow for the presence of oxygen vacancies in the first Ti–O shell. Thus, while the first shell appears fully occupied within experimental uncertainty, the possibility of oxygen vacancies beyond the first Er–O shell in the lattice cannot be ruled out.

The σ^2 factors indicate increased disorder beyond the first shell, particularly around the Er^{3+} ions, with a value of 0.0140 (5) Å² for the Er–Ti₍₁₎ distance. In addition, major differences between the data and simulations in the higher shells [Fig. 6(d)] point to erbium-driven structural changes beyond the first coordination shell, which may include oxygen vacancies located farther from the Er^{3+} sites. We were unable to model the Er local structure beyond the Er–Ti₍₁₎ distance. The long-range distortions in the local environment around Er^{3+} ions, extending to at least 4 Å, suggest that these defects are not isolated but cause widespread changes in the lattice. Even at 500 ppm doping levels, these extensive distortions may overlap, affecting a significant amount of Ti atoms, as suggested by the Ti K- and L-edge probes.

Finally, revisiting the PLE discussion, the observed decrease in the photoluminescence lifetime of Er^{3+} can be attributed to the dopant-induced generation of oxygen vacancies. These point defects act as non-radiative recombination centers, enabling energy transfer between Er^{3+} ions and oxygen vacancy defects, which leads to a quenching effect. Consequently, the photoluminescence lifetime decreases due to enhanced non-radiative recombination pathways. Since the photoluminescence lifetime imposes an upper limit on coherence time in quantum systems, the observed reduction in photoluminescence lifetimes indicates a corresponding decrease in coherence times. Other potential sources of non-radiative quenching, such as domain-associated defects or crystal field distortions, may also contribute to this effect and require further investigation to fully elucidate their roles.

IV. CONCLUSION

In conclusion, our investigation into epitaxial Er-doped rutile TiO_2 thin films reveals significant effects of erbium doping on both structural and electronic properties. XAS analysis at the O K-edge indicates that erbium doping leads to the formation of oxygen vacancies, which alter the electronic structure of the host lattice. EXAFS analysis for the Er L_3 -edge spectra indicates that Er^{3+} ions substitute for Ti^{4+} ions in the TiO_2 lattice. This substitution results in notable lattice distortions due to the larger ionic radius of Er^{3+} compared to Ti^{4+} . Coordination number analysis reveals consistent sixfold coordination around erbium, suggesting that neighboring oxygen ions stabilize the local charge environment. However, while our findings indicate significant distortions in higher-order shells, which may be associated with oxygen vacancies displaced from the first shell, further comparative studies are necessary to definitively determine the exact substitution sites. The broadening of the f–f excitation observed in PLE suggests a distribution of crystal fields, indicating structural disorder extending beyond the first coordination shell. This disorder impacts the crystal field sensed by the 4f electrons. The lattice distortions and additional point defects are expected to enhance non-radiative energy transfer, which correlates with the reduced photoluminescence lifetimes observed by PLE. This underscores the complex interplay between dopant-induced structural modifications and optical properties, emphasizing the importance of detailed local electronic and crystal structure investigations for advancing quantum information processing technologies.

ACKNOWLEDGMENTS

This work was supported by Q-NEXT, a U.S. Department of Energy Office of Science National Quantum Information Science Research Centers under Award No. DE-FOA-0002253. The use of the Advanced Photon Source, Argonne National Laboratory was

06 December 2024 17:15:27

supported by the U.S. Department of Energy, Office of Science, Basic Energy Sciences, under Contract No. DE-AC02-06CH11357.

AUTHOR DECLARATIONS

Conflict of Interest

The authors have no conflicts to disclose.

Author Contributions

J. B. Martins: Conceptualization (equal); Data curation (lead); Formal analysis (equal); Investigation (equal); Methodology (equal); Validation (equal); Visualization (lead); Writing – original draft (lead); Writing – review & editing (equal). **G. Grant:** Data curation (equal); Formal analysis (equal); Investigation (equal); Methodology (equal); Validation (equal); Visualization (equal); Writing – original draft (equal); Writing – review & editing (equal). **D. Haskell:** Data curation (equal); Formal analysis (equal); Methodology (equal); Validation (equal); Visualization (equal); Writing – original draft (equal); Writing – review & editing (equal). **G. E. Sterbinsky:** Data curation (equal); Investigation (supporting); Methodology (equal); Validation (equal); Visualization (equal); Writing – review & editing (equal). **I. Masiulionis:** Data curation (supporting); Validation (supporting); Visualization (supporting). **K. E. Sautter:** Conceptualization (equal); Investigation (supporting); Methodology (equal); Visualization (equal). **E. Karapetrova:** Data curation (equal); Methodology (equal). **S. Guha:** Funding acquisition (equal); Visualization (equal); Writing – review & editing (equal). **J. W. Freeland:** Conceptualization (equal); Data curation (equal); Formal analysis (equal); Funding acquisition (equal); Investigation (equal); Methodology (equal); Project administration (equal); Resources (equal); Supervision (equal); Validation (equal); Visualization (equal); Writing – original draft (equal); Writing – review & editing (equal).

DATA AVAILABILITY

The data that support the findings of this study are available within this article.

REFERENCES

- ¹D. D. Awschalom, R. Hanson, J. Wrachtrup, and B. B. Zhou, “Quantum technologies with optically interfaced solid-state spins,” *Nat. Photonics* **12**, 516–527 (2018).
- ²A. Laucht, F. Hohls, N. Ubbelohde, M. Fernando Gonzalez-Zalba, D. J. Reilly, S. Stobbe, T. Schröder, P. Scarlino, J. V. Koski, A. Dzurak, C.-H. Yang, J. Yoneda, F. Kuemmeth, H. Bluhm, J. Pla, C. Hill, J. Salfi, A. Oiwa, J. T. Muhonen, E. Verhagen, M. D. LaHaye, H. H. Kim, A. W. Tsen, D. Culcer, A. Geresdi, J. A. Mol, V. Mohan, P. K. Jain, and J. Baugh, “Roadmap on quantum nanotechnologies,” *Nanotechnology* **32**, 162003 (2021).
- ³A. Acín, I. Bloch, H. Buhrman, T. Calarco, C. Eichler, J. Eisert, D. Esteve, N. Gisin, S. J. Glaser, F. Jelezko, S. Kuhr, M. Lewenstein, M. F. Riedel, P. O. Schmidt, R. Thew, A. Wallraff, I. Walmsley, and F. K. Wilhelm, “The quantum technologies roadmap: A European community view,” *New J. Phys.* **20**, 080201 (2018).
- ⁴D. P. DiVincenzo, “Quantum computation,” *Science* **270**, 255–261 (1995).
- ⁵G. Zhang, Y. Cheng, J.-P. Chou, and A. Gali, “Material platforms for defect qubits and single-photon emitters,” *Appl. Phys. Rev.* **7**, 031308 (2020).

- ⁶G. Wolfowicz, F. J. Heremans, C. P. Anderson, S. Kanai, H. Seo, A. Gali, G. Galli, and D. D. Awschalom, “Quantum guidelines for solid-state spin defects,” *Nat. Rev. Mater.* **6**, 906–925 (2021).
- ⁷T. Zhong and P. Goldner, “Emerging rare-earth doped material platforms for quantum nanophotonics,” *Nanophotonics* **8**, 2003–2015 (2019).
- ⁸T. Böttger, C. W. Thiel, R. L. Cone, and Y. Sun, “Effects of magnetic field orientation on optical decoherence in $\text{Er}^{3+}:\text{Y}_2\text{SiO}_5$,” *Phys. Rev. B* **79**, 115104 (2009).
- ⁹D. Serrano, S. K. Kuppusamy, B. Heinrich, O. Fuhr, D. Hunger, M. Ruben, and P. Goldner, “Ultra-narrow optical linewidths in rare-earth molecular crystals,” *Nature* **603**, 241–246 (2022).
- ¹⁰A. M. Dibos, M. T. Solomon, S. E. Sullivan, M. K. Singh, K. E. Sautter, C. P. Horn, G. D. Grant, Y. Lin, J. Wen, F. J. Heremans, S. Guha, and D. D. Awschalom, “Purcell enhancement of erbium ions in TiO_2 on silicon nanocavities,” *Nano Lett.* **22**, 6530–6536 (2022).
- ¹¹M. Rančić, M. P. Hedges, R. L. Ahlfeldt, and M. J. Sellars, “Coherence time of over a second in a telecom-compatible quantum memory storage material,” *Nat. Phys.* **14**, 50–54 (2018).
- ¹²C. Ji, M. T. Solomon, G. D. Grant, K. Tanaka, M. Hua, J. Wen, S. K. Seth, C. P. Horn, I. Masiulionis, M. K. Singh, S. E. Sullivan, F. J. Heremans, D. D. Awschalom, S. Guha, and A. M. Dibos, “Nanocavity-mediated Purcell enhancement of Er in TiO_2 thin films grown via atomic layer deposition,” *ACS Nano* **18**(14), 9929–9941 (2024).
- ¹³P. Stevenson, C. M. Phenicie, I. Gray, S. P. Horvath, S. Welinski, A. M. Ferrenti, A. Ferrier, P. Goldner, S. Das, R. Ramesh, R. J. Cava, N. P. de Leon, and J. D. Thompson, “Erbium-implanted materials for quantum communication applications,” *Phys. Rev. B* **105**, 224106 (2022).
- ¹⁴T. Xie, J. Rochman, J. G. Bartholomew, A. Ruskuc, J. M. Kindem, I. Craiciu, C. W. Thiel, R. L. Cone, and A. Faraon, “Characterization of $\text{Er}^{3+}:\text{YVO}_4$ for microwave to optical transduction,” *Phys. Rev. B* **104**, 054111 (2021).
- ¹⁵C. M. Phenicie, P. Stevenson, S. Welinski, B. C. Rose, A. T. Asfaw, R. J. Cava, S. A. Lyon, N. P. de Leon, and J. D. Thompson, “Narrow optical line widths in erbium implanted in TiO_2 ,” *Nano Lett.* **19**, 8928–8933 (2019).
- ¹⁶K. Shin, I. Gray, G. Marcaud, S. P. Horvath, F. J. Walker, J. D. Thompson, and C. H. Ahn, “Er-doped anatase TiO_2 thin films on LaAlO_3 (001) for quantum interconnects (QulCs),” *Appl. Phys. Lett.* **121**, 081902 (2022).
- ¹⁷M. K. Singh, G. Wolfowicz, J. Wen, S. E. Sullivan, A. Prakash, A. M. Dibos, D. D. Awschalom, F. J. Heremans, and S. Guha, “Development of a scalable quantum memory platform—Materials science of erbium-doped TiO_2 thin films on silicon,” *J. Appl. Phys.* **136**(12), 124402 (2024).
- ¹⁸B. Jalan, R. Engel-Herbert, J. Cagnon, and S. Stemmer, “Growth modes in metal-organic molecular beam epitaxy of TiO_2 on r-plane sapphire,” *J. Vac. Sci. Technol., A* **27**, 230–233 (2009).
- ¹⁹A. L. Ankudinov, B. Ravel, J. J. Rehr, and S. D. Conradson, “Real-space multiple-scattering calculation and interpretation of x-ray-absorption near-edge structure,” *Phys. Rev. B* **58**, 7565–7576 (1998).
- ²⁰R. Engel-Herbert, B. Jalan, J. Cagnon, and S. Stemmer, “Microstructure of epitaxial rutile TiO_2 films grown by molecular beam epitaxy on r-plane Al_2O_3 ,” *J. Cryst. Growth* **312**, 149–153 (2009).
- ²¹J. YHuang, B. H. Park, D. Jan, X. Q. Pan, Y. T. Zhu, and Q. X. Jia, “High-resolution transmission electron microscopy study of defects and interfaces in epitaxial TiO_2 films on sapphire and LaAlO_3 ,” *Philos. Mag. A* **82**, 735–749 (2002).
- ²²G. D. Grant, J. Zhang, I. Masiulionis, S. Chattaraj, K. E. Sautter, S. E. Sullivan, R. Chebrolu, Y. Liu, J. B. Martins, J. Niklas, A. M. Dibos, S. Kewalramani, J. W. Freeland, J. Wen, O. G. Poluektov, F. J. Heremans, D. D. Awschalom, and S. Guha, “Optical and microstructural characterization of Er^{3+} doped epitaxial cerium oxide on silicon,” *APL Mater.* **12**, 021121 (2024).
- ²³A. M. Stoneham, “Shapes of inhomogeneously broadened resonance lines in solids,” *Rev. Mod. Phys.* **41**, 82–108 (1969).
- ²⁴S. Obregón, A. Kubacka, M. Fernández-García, and G. Colón, “High-performance $\text{Er}^{3+}-\text{TiO}_2$ system: Dual up-conversion and electronic role of the lanthanide,” *J. Catal.* **299**, 298–306 (2013).
- ²⁵J. B. Pérez, M. Courel, R. C. Valderrama, I. Hernández, M. Pal, F. P. Delgado, and N. Mathews, “Structural, optical, and photoluminescence properties of erbium doped TiO_2 films,” *Vacuum* **169**, 108873 (2019).

- ²⁶L. Minervini, M. O. Zacate, and R. W. Grimes, "Defect cluster formation in M_2O_3 -doped CeO_2 ," *Solid State Ionics* **116**, 339–349 (1999).
- ²⁷D. T. Cromer and K. Herrington, "The structures of anatase and rutile," *J. Am. Chem. Soc.* **77**, 4708–4709 (1955).
- ²⁸R. Ruus, A. Kikas, A. Saar, A. Ausmees, E. Nõmmiste, J. Aarik, A. Aidla, T. Uustare, and I. Martinson, "Ti 2p and O 1s X-ray absorption of TiO_2 polymorphs," *Solid State Commun.* **104**, 199–203 (1997).
- ²⁹Y. Harada, T. Kinugasa, R. Eguchi, M. Matsubara, A. Kotani, M. Watanabe, A. Yagishita, and S. Shin, "Polarization dependence of soft-x-ray Raman scattering at the L edge of TiO_2 ," *Phys. Rev. B* **61**, 12854–12859 (2000).
- ³⁰B. Jiang, J. M. Zuo, N. Jiang, M. O'Keeffe, and J. C. H. Spence, "Charge density and chemical bonding in rutile TiO_2 ," *Acta Crystallogr., Sect. A: Found. Crystallogr.* **59**, 341–350 (2003).
- ³¹P.-H. Hsieh, Y.-M. Lu, W.-S. Hwang, W.-L. Jang, C.-L. Dong, and T.-S. Chan, "X-ray absorption spectroscopy study of thermally annealed Cu–Al–O thin films," *Mater. Chem. Phys.* **144**, 547–552 (2014).
- ³²G. C. Vázquez, S. Z. Karazhanov, D. Maestre, A. Cremades, J. Piqueras, and S. E. Foss, "Oxygen vacancy related distortions in rutile TiO_2 nanoparticles: A combined experimental and theoretical study," *Phys. Rev. B* **94**, 235209 (2016).
- ³³F. De Angelis, C. Di Valentin, S. Fantacci, A. Vittadini, and A. Selloni, "Theoretical studies on anatase and less common TiO_2 phases: Bulk, surfaces, and nanomaterials," *Chem. Rev.* **114**, 9708–9753 (2014).
- ³⁴E. G. Seebauer and M. C. Kratzer, "Charged point defects in semiconductors," *Mater. Sci. Eng., R* **55**, 57–149 (2006).
- ³⁵F. M. F. de Groot, J. C. Fuggle, B. T. Thole, and G. A. Sawatzky, " $L_{2,3}$ x-ray-absorption edges of d^0 compounds: K^+ , Ca^{2+} , Sc^{3+} , and Ti^{4+} in O_h (octahedral) symmetry," *Phys. Rev. B* **41**, 928–937 (1990).
- ³⁶P. Krüger, "Multichannel multiple scattering calculation of $L_{2,3}$ -edge spectra of TiO_2 and $SrTiO_3$: Importance of multiplet coupling and band structure," *Phys. Rev. B* **81**, 125121 (2010).
- ³⁷W. Li, A. I. Frenkel, J. C. Woicik, C. Ni, and S. I. Shah, "Dopant location identification in Nd^{3+} -doped TiO_2 nanoparticles," *Phys. Rev. B* **72**, 155315 (2005).
- ³⁸G. C. Vázquez, D. Maestre, A. Cremades, J. Ramírez-Castellanos, E. Magnano, S. Nappini, and S. Z. Karazhanov, "Understanding the effects of Cr doping in rutile TiO_2 by DFT calculations and X-ray spectroscopy," *Sci. Rep.* **8**, 8740 (2018).
- ³⁹B. T. Thole, G. v. d. Laan, J. C. Fuggle, G. A. Sawatzky, R. C. Karnatak, and J.-M. Esteve, "3d x-ray-absorption lines and the $3d^9 4f^{n+1}$ multiplets of the lanthanides," *Phys. Rev. B* **32**, 5107–5118 (1985).
- ⁴⁰R. Shannon and C. Prewitt, "Effective ionic radii in oxides and fluorides," *Acta Crystallogr., Sect. B* **25**, 925–946 (1969).
- ⁴¹W. Luo, C. Fu, R. Li, Y. Liu, H. Zhu, and X. Chen, " Er^{3+} -Doped anatase TiO_2 nanocrystals: Crystal-field levels, excited-state dynamics, upconversion, and defect luminescence," *Small* **7**, 3046–3056 (2011).
- ⁴²Z. Rao, X. Xie, X. Wang, A. Mahmood, S. Tong, M. Ge, and J. Sun, "Defect chemistry of Er^{3+} -doped TiO_2 and its photocatalytic activity for the degradation of flowing gas-phase VOCs," *J. Phys. Chem. C* **123**, 12321–12334 (2019).